



## Article

# Optimization of MHD Flow of Radiative Micropolar Nanofluid in a Channel by RSM: Sensitivity Analysis

Reham A. Alahmadi <sup>1</sup>, Jawad Raza <sup>2,\*</sup>, Tahir Mushtaq <sup>2</sup>, Shaimaa A. M. Abdelmohsen <sup>3</sup>, Mohammad R. Gorji <sup>4</sup> and Ahmed M. Hassan <sup>5</sup>

<sup>1</sup> Basic Science Department, College of Science and Theoretical Studies, Saudi Electronic University, Riyadh 11673, Saudi Arabia

<sup>2</sup> Department of Mathematics, COMSATS University Islamabad, Vehari Campus, Vehari 61100, Pakistan

<sup>3</sup> Department of Physics, College of Science, Princess Nourah Bint Abdulrahman University, P.O. Box 84428, Riyadh 11671, Saudi Arabia

<sup>4</sup> Faculty of Medicine and Health Sciences, Ghent University, 9000 Ghent, Belgium

<sup>5</sup> Department of Mechanical Engineering, Future University in Egypt, New Cairo 11835, Egypt

\* Correspondence: jawadraza@cuivehari.edu.pk

**Abstract:** These days, heat transfer plays a significant role in the fields of engineering and energy, particularly in the biological sciences. Ordinary fluid is inadequate to transfer heat in an efficient manner, therefore, several models were considered for the betterment of heat transfer. One of the most prominent models is a single-phase nanofluid model. The present study is devoted to solving the problem of micropolar fluid with a single-phase model in a channel numerically. The governing partial differential equations (PDEs) are converted into nonlinear ordinary differential equations (ODEs) by introducing similarity transformation and then solved numerically by the finite difference method. Response surface methodology (RSM) together with sensitivity analysis are implemented for the optimization analysis. The study reveals that sensitivity of the skin friction coefficient ( $C_{fx}$ ) to the Reynolds number ( $R$ ) and magnetic parameter ( $M$ ) is positive (directly proportional) and negative (inversely proportional) for the micropolar parameter.



**Citation:** Alahmadi, R.A.; Raza, J.; Mushtaq, T.; Abdelmohsen, S.A.M.; R. Gorji, M.; Hassan, A.M. Optimization of MHD Flow of Radiative Micropolar Nanofluid in a Channel by RSM: Sensitivity Analysis. *Mathematics* **2023**, *11*, 939. <https://doi.org/10.3390/math11040939>

Academic Editor: Ramoshweu Solomon Lebelo

Received: 3 January 2023

Revised: 8 February 2023

Accepted: 10 February 2023

Published: 13 February 2023



**Copyright:** © 2023 by the authors. Licensee MDPI, Basel, Switzerland. This article is an open access article distributed under the terms and conditions of the Creative Commons Attribution (CC BY) license (<https://creativecommons.org/licenses/by/4.0/>).

**Keywords:** micropolar fluid; nanofluid; thermal radiation; response surface methodology; sensitivity analysis

**MSC:** 76D55

## 1. Background

In previous decades, a demand to represent the fluid that depends on micro-components has concluded in the establishment of micropolar fluid. Eringen [1,2] was the first researcher to use the term micropolar. This term then became an area of dynamic exploration. A simple microfluid, by definition, is a fluent medium whose properties and actions in each of its volume elements are influenced by local movements of the material particles; such a fluid has local inertia. Eringen [2] presents a complete discussion of motion and micro-motions in the presentation of the theory, as well as evidence of the newly introduced micro-deformation rate tensors, which is a prerequisite for the creation of the constitutive equations used to characterise a simple microfluid. These classes of fluids identify many engineering and industrial applications physically and mathematically. On the other hand, a class of conventional Newtonian fluids cannot specifically identify the fluid flow for a range of applications in the area of engineering. The examples of such fluids are polymeric, colloidal solutions, paints, etc. In micropolar fluid, the micro-rotation vectors explain the rotational motion in microfluid. Therefore, the curl of the velocity vector in this case will be non-zero.

The control of magnetic induction past a plate in the existence of a micropolar fluid have mainly been evaluated by Gorla and Mohammedain [3]. Pedieson [4] evaluated and

studied boundary layer theory of micropolar fluids. Gupta [5] pursued this work in a study in which they examined the impact of the transmission of the heat of a fluid over a surface that was stretched. The flow of fluid across a stretched surface was then determined in order to do further research on Gupta's work [6].

### 1.1. Literature Review

The importance of heat transfer and heat exchangers cannot be overstated. For instance, raising the temperature will be necessary to increase the efficiency of the thermal processes for the production of heat and electricity [7,8]. The transfer of energy from one place (high concentration) to another place (low concentration) is known as heat transfer. Applications of heat transportation can be seen in our daily lives; for example, the human body emits heat continuously, and adjustment of the human body temperature is achieved by using clothing to adapt changing climatic conditions. Heat transportation is also utilised to manage temperature in our structures [9] and is required for cooking, refrigeration, and drying. It is also utilised for temperature regulation in automotive radiators [10] and mobile devices [11]. Solar thermal collectors [12,13] and spaceship thermal control elements [14] use heat conversion to turn solar energy into heat and power. Many of these systems require rapid heat dissipation to enable successful performance and optimum productivity inside the system [15]. As modern sciences progress, devices have become tiny, necessitating preferable temperature control. Basically, the smaller the scale, the more efficient cooling technology is required [16]. In thermal engineering, heat transfer enhancement is therefore a very important field.

Choi and Eastman [17] prepared nanofluids, which are colloidal suspensions of nano-scale metallic or non-metallic particles in a host fluid (HF). There are few fundamental conditions which met, low agglomeration of nanoparticles and steady-state suspension and the HF should be chemically constant. Nanofluids have two subcategories: non-metallic nanofluids (carbides: carbon, TiC, materials: SWCNT/MWCNT, graphene, diamond, etc.) and metallic nanofluids (metals: Cu, Fe, Al, Ag, Au; metal oxides: SiO<sub>2</sub>, Al<sub>2</sub>O<sub>3</sub>, TiO<sub>2</sub>, CuO). There are two methods to develop nanofluid: a one-step method, which involves developing the HF and nanoparticles at the same time; and the two-step method, in which it is generated separately and then mixed up [18]. For several applications, nanofluids have important properties, such as good stability, high heat conductivity, reduced erosion and friction coefficient, ultrafast heat transfer ability, and good lubrication.

Mathematical simulations by Rashid et al. [19] showed the combined effects of an angled magnetic field and a predetermined surface temperature (PST) on Cu-Al<sub>2</sub>O<sub>3</sub>-type nanoparticles in water. They found that the temperature rises by solid volume fraction  $\phi$ , magnetic parameter  $M$ , and slip-parameter for both Cu-H<sub>2</sub>O and Al<sub>2</sub>O<sub>3</sub>-H<sub>2</sub>O. Haq and Aman [20] quantitatively evaluated the thermal performance of a water-based copper oxide (CuO) nanofluid in a trapezoidal cavity with the use of the finite element method (FEM). They concluded from this investigation that the velocity steadily decreases as the fluid thickens and becomes denser due to the presence of a solid volume fraction ( $=0-0.2$ ). In a similar way, the rate of heat transmission is likewise decreasing as  $=0-0.2$  increases, owing to convection. The characteristics of non-uniform melting heat transmission of a nanofluid over a sheet were investigated by Hayat et al. [21]. The base fluid (water, H<sub>2</sub>O) was injected with copper (Cu) nanoparticles, and HAM was used to solve a governing self-similar system of differential equations. In this investigation, they found that when the volume fraction, Hartman number, and porosity parameter values increased, so did the skin friction coefficient and local Nusselt number. The effects of heat transmission on aluminium alloy nanoparticles suspended across a sheet under the influence of a magnetic field were studied by Sandeep et al. [22]. They took into consideration two distinct kinds of nanoparticles, AA 7072 (98% Al, 1% Zn, and 1% additives) and AA 7075 (90% Al, 5.6 Zn, 2.3 Mg, 1.2 Cu, and additives). Due to a larger proportion of copper used, the mathematical research revealed that AA 7075 had a substantially higher heat transfer rate than AA 7072. (Cu).

Shah et al. [23] conducted a mathematical investigation of aluminium and ethylene glycol nanoparticles on a sheet while taking the second law of thermodynamics into account.

### 1.2. Motivations

The great efforts and expertise of the researchers have succeeded in publishing the results of fluid flow between confined parallel plates. Suitable similar variables and numerical approaches were adopted in order to generate the results. The following constituents give the motivations of this research work.

- The problem of viscoelastic fluid in a confined space (channel) with extending walls was discussed by Misra et al. [24]. According to the study, reverse flow occurs close to the region's (channel's) centre and can be managed by applying an external magnetic field.
- Ashraf et al. [25] looked into the issue of micropolar fluid flow with heat transmission in a channel with stretching walls. Equations of fourth order coupled nonlinear ordinary differential type were solved using the quasi-linearization approach. The study exposed the fact that shear, coupled stresses and heat transfer rate at the walls are increased by stretching the channel walls. They also quantified that their investigation may be valuable for the flow and thermal control of polymeric processing.
- Researcher [26–28] examined the effect of heat transfer and nanoparticles on MHD water/kerosene-based nanofluid in a channel numerically. The studies revealed the fact that there exists a linear relationship between the thermal boundary layer thickness and the solid volume fraction.

The above-mentioned motivations of the study are either a problem of simple micropolar fluid or simple nanofluid in a channel with stretching walls. Therefore, without any doubt, it can be argued that there exists a potential research gap to investigate the problem related to micropolar nanofluid flow in a channel with stretching/shrinking walls.

### 1.3. Contributions

The following items are the main contribution of the current research.

- It proposes the single-phase nanofluid model of micropolar copper–blood nanoparticles in a channel with stretching and shrinking walls.
- Thermal radiations are also present in the channel to make the problem more appealing for heat transfer.
- To control the reversibility of the flow due to the stretching walls, we impose a transverse magnetic field.
- This research also investigates sensitivity analysis using response surface methodology (RSM).

## 2. Proposed Model

Consider two-dimensional steady laminar incompressible micropolar nanofluid in a channel with stretching and shrinking walls in the presence of a magnetic field and thermal radiation. In this study, copper nanoparticles are the solid dispersed phase while blood is the fluid continuum phase. The lower and upper walls of the channel stretch and shrink in the direction of the fluid ( $x$ -axis) with some constant rate  $u = bx \forall b \in R$ . If  $b > 0$ , then the case is known as stretching and  $b < 0$  is for shrinking walls of the channel (see Figure 1).

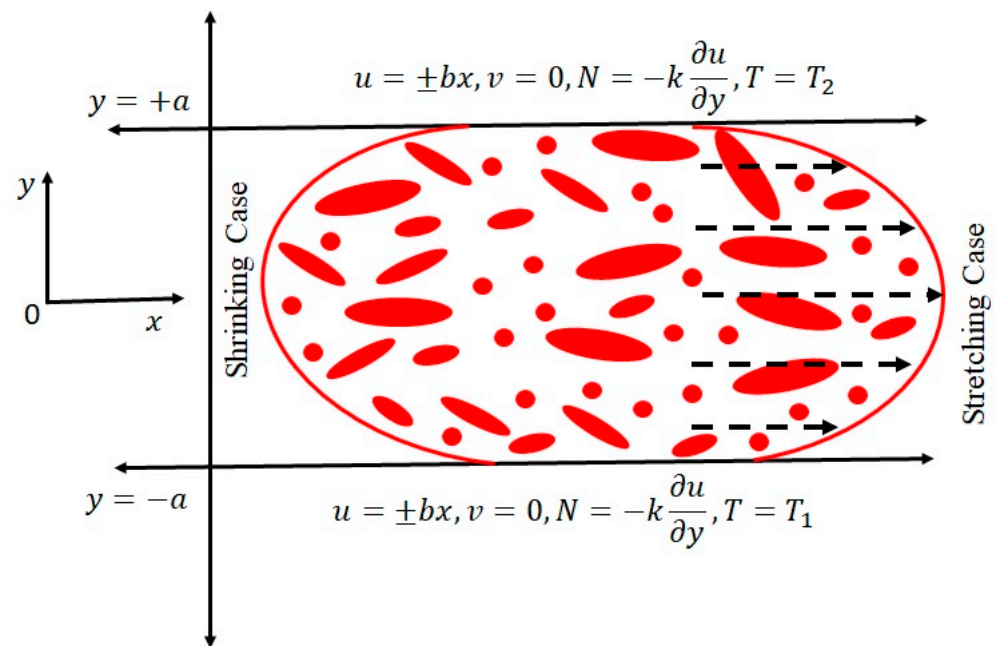


**Figure 1.** Physical sketch of the problem.

### 2.1. Governing Equations

The general equations of micropolar fluids as given by Eringen [1] can be represented in component form  $\bar{V} = (u(x, y), v(x, y), 0)$ ,  $\bar{v} = (0, 0, N(x, y))$ , where  $N = \nabla \times V \neq 0$  as:

$$\frac{\partial u}{\partial x} + \frac{\partial v}{\partial y} = 0 \quad (1)$$

$$u \frac{\partial u}{\partial x} + v \frac{\partial u}{\partial y} = \frac{-1}{\rho} \frac{\partial p}{\partial x} + \frac{\mu + \kappa}{\rho} \nabla^2 u + \frac{\kappa}{\rho} \frac{\partial N}{\partial y} - \frac{\sigma_f B_o^2}{\rho_{nf}} u \quad (2)$$

$$\frac{\partial v}{\partial x} + v \frac{\partial v}{\partial y} = \frac{-1}{\rho} \frac{\partial p}{\partial y} + \frac{\mu + \kappa}{\rho} \nabla^2 v - \frac{\kappa}{\rho} \frac{\partial N}{\partial x} \quad (3)$$

$$\rho_{nf} j \left( u \frac{\partial N}{\partial x} + v \frac{\partial N}{\partial y} \right) = \gamma_{nf} \nabla^2 N + \kappa \left( \frac{\partial v}{\partial x} - \frac{\partial u}{\partial y} \right) - 2\kappa N \quad (4)$$

$$\left( u \frac{\partial T}{\partial x} + v \frac{\partial T}{\partial y} \right) = \frac{k_{nf}}{(\rho C_p)_{nf}} \left( \frac{\partial^2 T}{\partial x^2} + \frac{\partial^2 T}{\partial y^2} \right) - \frac{1}{(\rho C_p)_{nf}} \frac{\partial q_r}{\partial y} \quad (5)$$

Here,  $p$  is the pressure,  $N$  is the micro-rotational velocity,  $\gamma_{nf} = j \left( \frac{\kappa}{2} + \mu_{nf} \right)$  is the spine gradient viscosity, and  $u$  and  $v$  are the axial and transverse velocities components, respectively. The appropriate boundary conditions for the current investigation are:

$$u = \pm bx, v = 0, N = -k \frac{\partial u}{\partial y}, T = T_1 \text{ at } y = -a \quad (6)$$

$$u = \pm bx, v = 0, N = -k \frac{\partial u}{\partial y}, T = T_2 \text{ at } y = +a \quad (7)$$

These physical quantities are described mathematically as:

$$\rho_{nf} = \rho_f (1 - \phi) + \phi \rho_s \quad (8)$$

$$\mu_{nf} = \frac{\mu_f}{(1 - \phi)^{2.5}} \quad (9)$$



$$(\rho C_p)_{nf} = (\rho C_p)_f(1 - \varphi) + (\rho C_p)_s \varphi \quad (10)$$

$$\frac{k_{nf}}{k_f} = \frac{k_s + 2k_f - 2\varphi(k_f - k_s)}{k_s + 2k_f + \varphi(k_f - k_s)} \quad (11)$$

Here,  $\varphi$  is the solid volume fraction,  $\varphi_s$  is for the nanosolid-particles, and  $\varphi_f$  is for the base fluid.

We apply a Rosseland approximation for radiation as:

$$q_r = -\frac{4\sigma^*}{3k^*} \frac{\partial T^4}{\partial y} \quad (12)$$

Here, the Stefan–Boltzmann constant is given by  $\sigma^* = 5.6697 \times 10^{-8} \text{ Wm}^{-2}\text{K}^{-4}$  and the mean spectral absorption coefficient is denoted by  $k^*$ . Further, blackbody emission power,  $eb$  in terms of the Stefan–Boltzmann constant and absolute temperature, is given by  $e_b = \sigma^* T^4$ .

It is assumed that the temperature differences within the flow, such as the term  $T^4$ , may be expressed as a linear function of temperature. We obtain the Taylor series expansion for  $T^4$  at a free stream temperature  $T_\infty$ .

$$T^4 = T_\infty^4 + 4T_\infty^3(T - T_\infty) + 8T_\infty^2(T - T_\infty)^2 + \dots$$

After neglecting higher-order terms as:

$$T^4 = 4T_\infty^4 T - 3T_\infty^4 \quad (13)$$

Using Equation (12) in (13), we obtain:

$$\frac{\partial q_r}{\partial y} = -\frac{16\sigma^* T_\infty^3}{3k^*} \frac{\partial^2 T}{\partial y^2} \quad (14)$$

Equation (5) is now converted in the light of (14) as:

$$(\rho C_p)_{nf} \left( u \frac{\partial T}{\partial x} + v \frac{\partial T}{\partial y} \right) = k_{nf} \left( \frac{\partial^2 T}{\partial x^2} + \frac{\partial^2 T}{\partial y^2} \right) + \frac{16\sigma^* T_\infty^3}{3k^*} \frac{\partial^2 T}{\partial y^2} \quad (15)$$

## 2.2. Similarity Solution

Now we introduce the similarity transformation as:

$$\eta = \frac{y}{a}, u = bxf'(\eta), v = -abf(\eta), \theta(\eta) = \frac{T - T_2}{T_1 - T_2} \quad (16)$$

Using Equation (16) in Equation (1), we see that Equation (1) is identically satisfied and eliminating the pressure term from (2) and (5), we obtain the required similarity coupled system of the ordinary differential equation as:

$$\left( 1 + \frac{\kappa}{\Gamma_2} \right) f'''' - \frac{\Gamma_1}{\Gamma_2} R(f'f'' - ff''') - \frac{\kappa}{\Gamma_2} g' - \frac{M^2}{\Gamma_2} f'' = 0 \quad (17)$$

$$\left( 1 + \frac{\kappa}{2\Gamma_2} \right) g'' + \frac{\kappa}{\Gamma_2} (f'' - 2g) + \frac{\Gamma_1}{\Gamma_2} R(fg' - f'g) = 0 \quad (18)$$

$$\frac{1}{\Gamma_3 Pr} \left( \Gamma_4 + \frac{4}{3} Rd \right) \theta'' + Rf\theta' = 0 \quad (19)$$

Subject to the boundary conditions:

$$f(-1) = 0, f'(-1) = \pm 1, g(-1) = 0, \theta(-1) = 1 \quad (20)$$

$$f(1) = 0, f'(1) = \pm 1, g(1) = 0, \theta(1) = 0 \quad (21)$$

Here,  $R = \frac{a^2 b}{\nu_f}$  is the Reynolds number,  $M^2 = \frac{\sigma_f B_0^2 a^2}{\mu_f}$  is the magnetic parameter,  $K = \frac{k}{\nu_f}$  is the micropolar parameter,  $Pr = \frac{\nu_f (\rho C_p)_f}{k_f}$  is the Prandtl number, and  $Rd = \frac{\sigma^* T_\infty^3}{3k^* k_f}$  is the radiation parameter. Also,

$$\Gamma_1 = (1 - \varphi) + \varphi \frac{\rho_s}{\rho_f}, \quad \Gamma_2 = \frac{1}{(1 - \varphi)^{2.5}},$$

$$\Gamma_3 = (1 - \varphi) + \frac{(\rho C_p)_s}{(\rho C_p)_f} \varphi, \quad \Gamma_4 = \frac{k_s + 2k_f - 2\varphi(k_f - k_s)}{k_s + 2k_f + \varphi(k_f - k_s)}$$

### 3. Results and Discussion

The numerical results have been handled in this section in the form of tables and graphs. Equations (17)–(19), subject to boundary conditions (20) and (21), are solved with the aid of a numerical scheme called Runge–Kutta 4th order and finite difference base scheme (bvp4c) [29]. Equations (17)–(19) are higher order ODEs, so we converted them into a system of first order ODEs, however three (03) initial conditions were missing  $\left( \frac{d^2 f}{d\eta^2} \Big|_{\eta=0}, \frac{d^3 f}{d\eta^3} \Big|_{\eta=0}, \frac{d^2 g}{d\eta^2} \Big|_{\eta=0}, \frac{d\theta}{d\eta} \Big|_{\eta=0} \right)$ . To find these missing initial conditions, we employed a shooting method. Once these missing conditions were found, then the solution computed and satisfied the boundary conditions (20) and (21). Thermophysical properties of blood and copper nanoparticles [27] are fetched from Table 1.

**Table 1.** Thermophysical properties of the blood and copper nanoparticles (see [27]).

Properties	Blood	Copper
Density $\left( \frac{\text{Kg}}{\text{m}^3} \right)$	1150	8933
Thermal conductivity $\left( \frac{\text{W}}{\text{mK}} \right)$	0.53	401
Specific Heat $\left( \text{JKg}^{-1}\text{K}^{-1} \right)$	3617	385

Figures 2–12 provide information on the hydrokinetic effects on velocity, angular velocity, temperature, and concentration. The comparison of the two different approaches of the numerical results is presented graphically in Figure 2 and it is depicted that the results coincide with each other. Figure 3 depicts how the micropolar parameter affects the velocity profile  $f'(\eta)$  for stretching and contracting the wall. The velocity profile, which is parabolic in character, is shown to decline as the micropolar parameter rises. However, we deduced from Figure 4 that the micro-rotation  $g(\eta)$  profile gradually increases as the micropolar parameter  $K$  increases after decreasing from the bottom wall to the channel centre. The micro-rotation profile displays an entirely different pattern in the case of diminishing walls. On other hand, the temperature profile  $\theta(\eta)$  rises while the walls are extending and falls when the walls are contracting. As can be observed from Figure 8, the velocity profile decreases as the solid volume percentage increases for stretching walls and rises for contracting walls. The impact of the stretching Reynolds number  $R$  on the velocity profile is explained in Figure 9. This graphic demonstrates how the velocity profile for the stretched walls reduces towards the channel borders and increases near the channel centre. However, it can be seen in Figure 10 that the micro-rotation profile rises from the lower wall to the channel's centre, and then falls when the values of the Reynolds number for the

stretched walls are raised. Figure 11 also illustrates the effect of the Reynolds number on the temperature profile. We can observe that the temperature profile changes for the bottom and upper halves of the channel when the Reynolds number values are increased. Figure 12 shows the effect of the radiation parameter on the temperature profile. The temperature profile of the tube drops from the lower wall to the middle and climbs from the centre to the top wall as the radiation parameter rises. The reverse result, however, can be seen in the case of the diminishing walls.

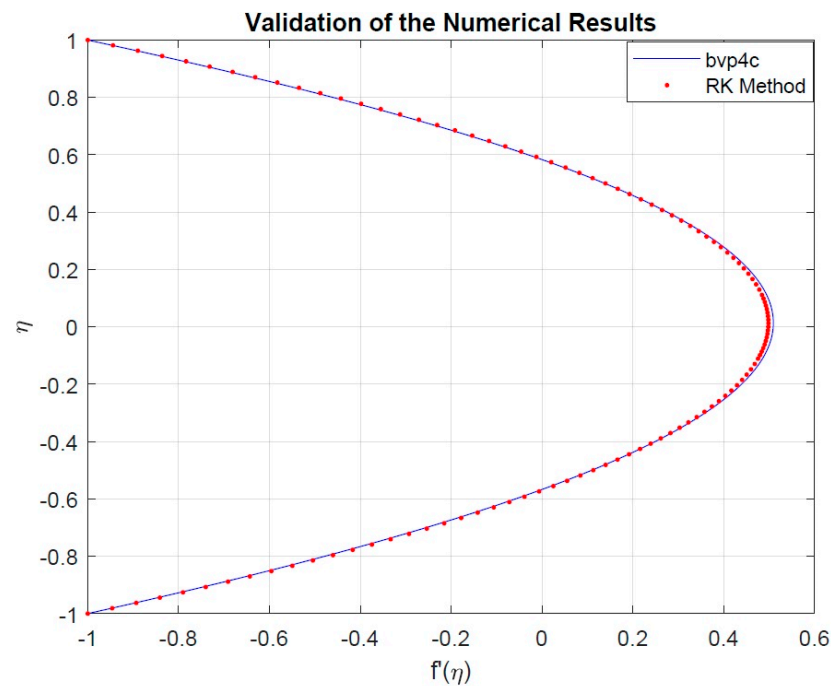


Figure 2. Code verification.

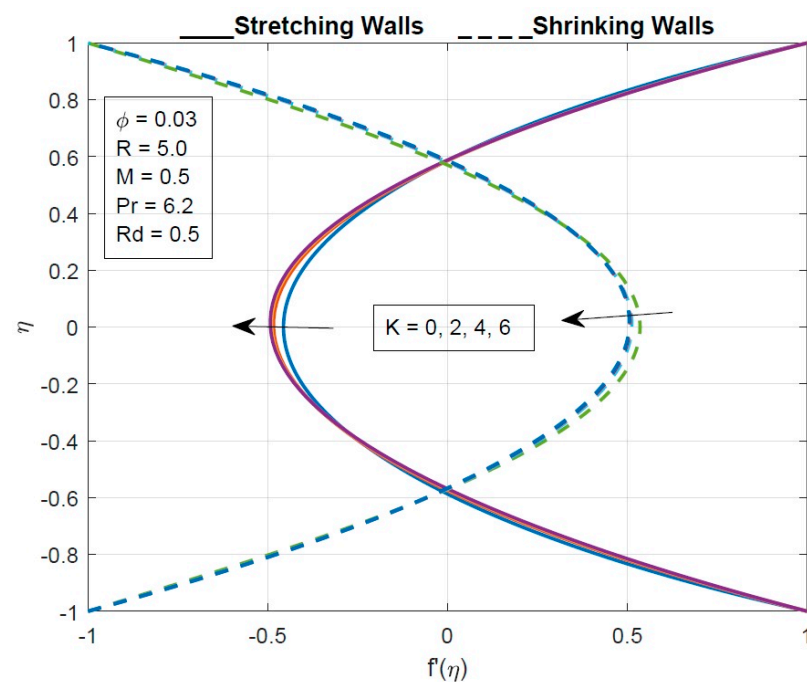
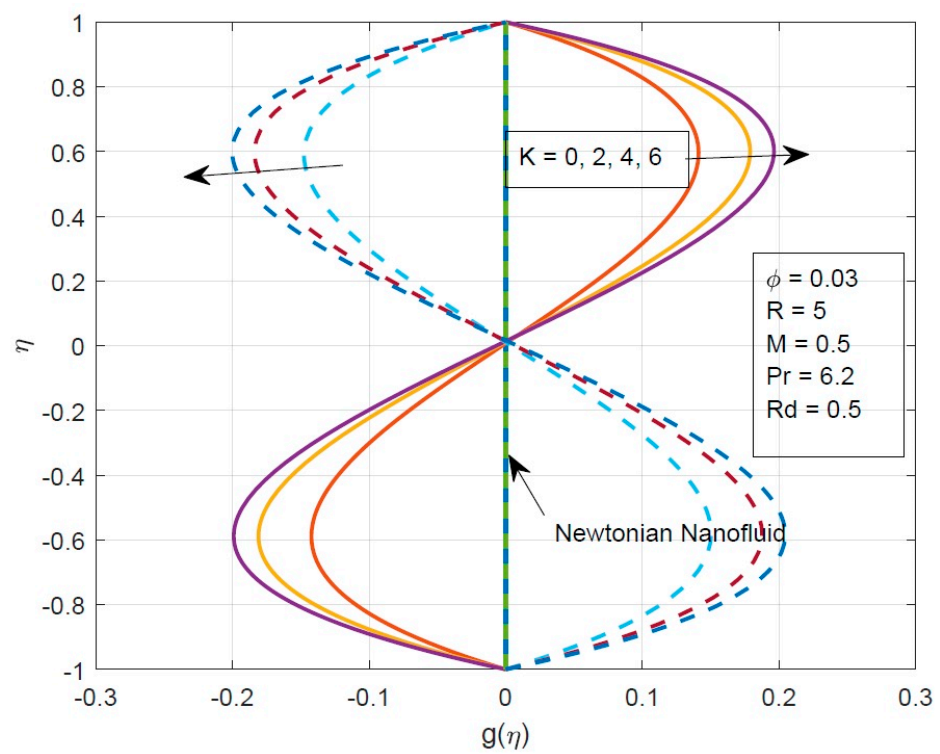
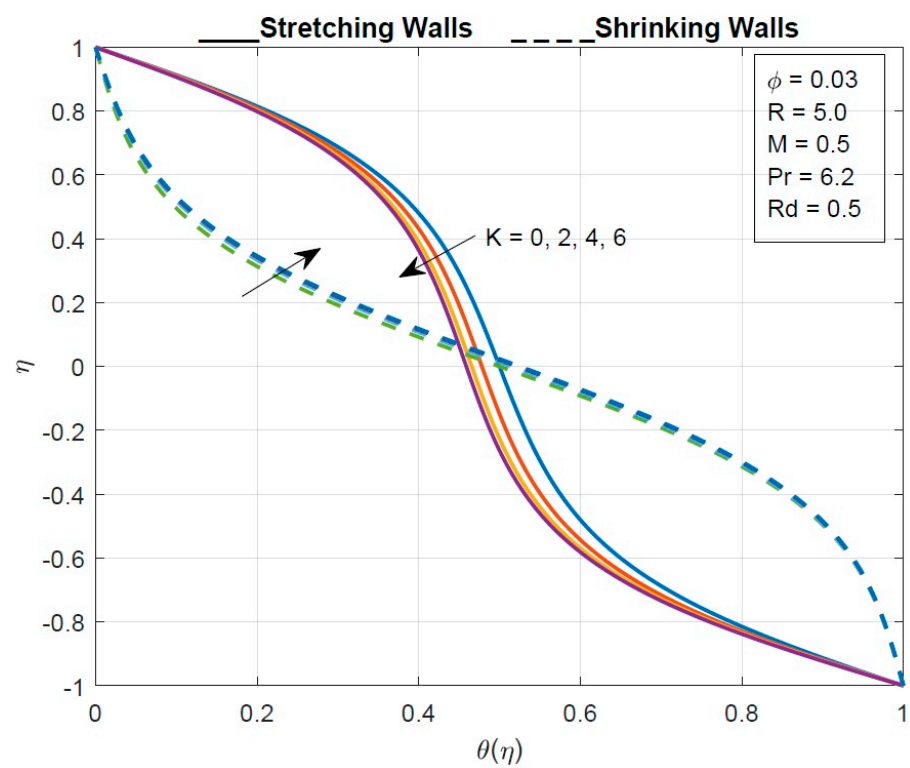


Figure 3. The effect of the micropolar parameter on the velocity profile.



**Figure 4.** The effect of the micropolar parameter on the micro-rotation.



**Figure 5.** The effect of the micropolar parameter on the temperature profile.

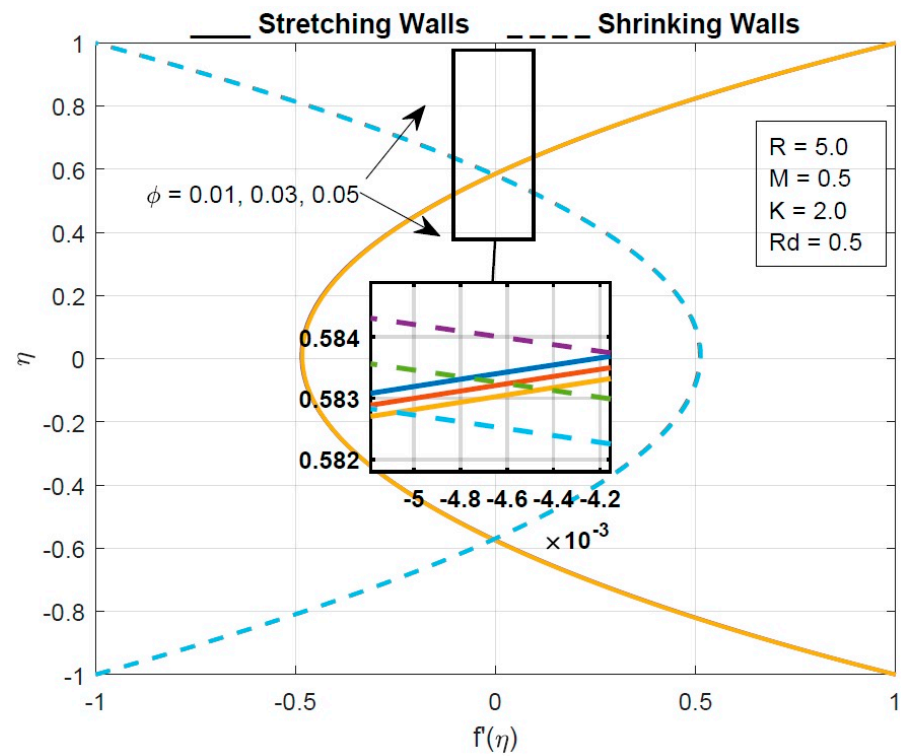


**Figure 6.** The effect of the solid volume fraction on the velocity profile.

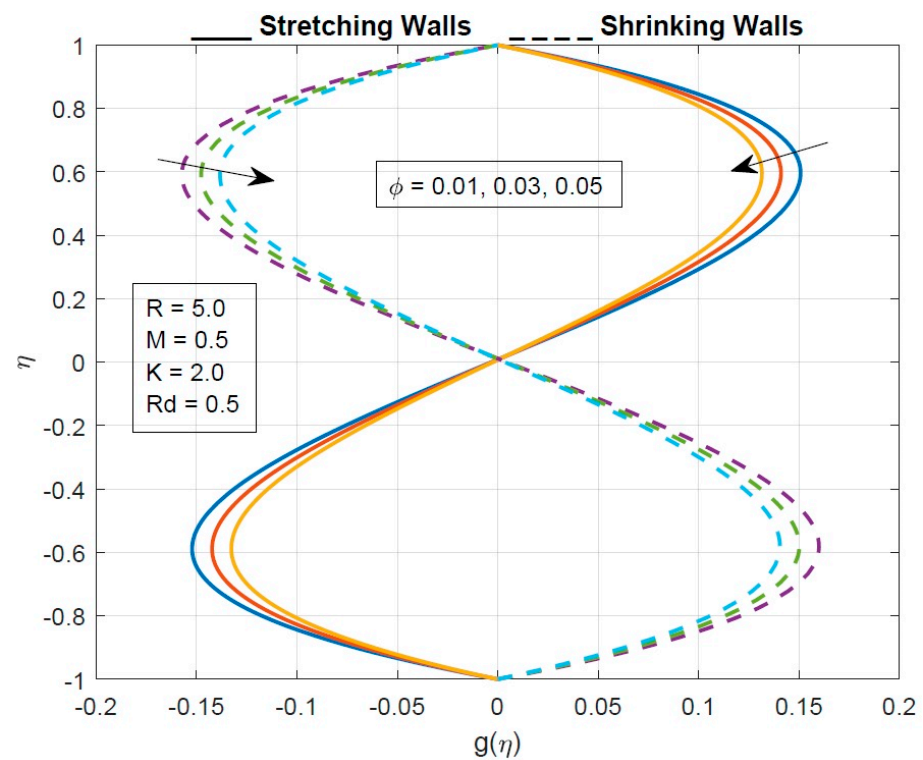


**Figure 7.** The effect of the solid volume fraction on the micro-rotation profile.

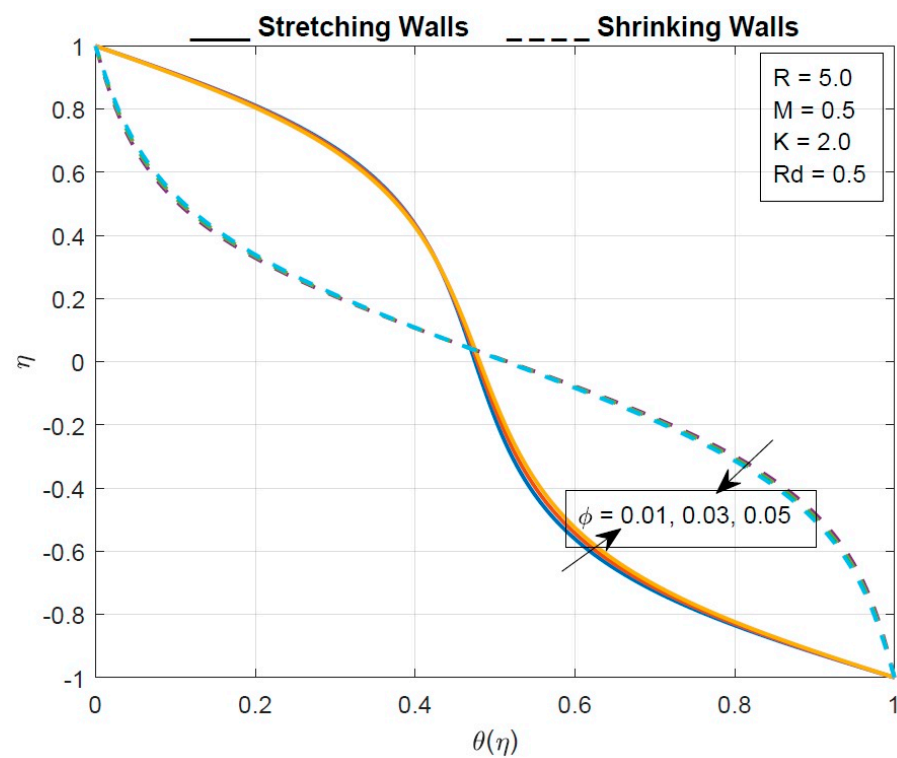


**Figure 8.** The effect of the solid volume fraction on the temperature profile.

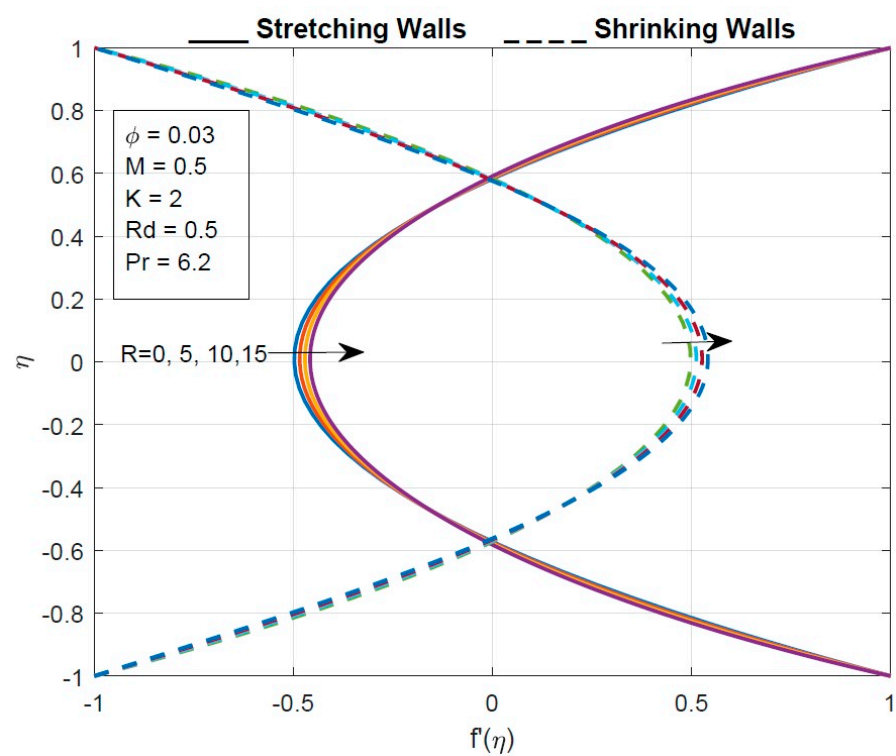


**Figure 9.** The effect of the Reynolds number on the velocity profile.



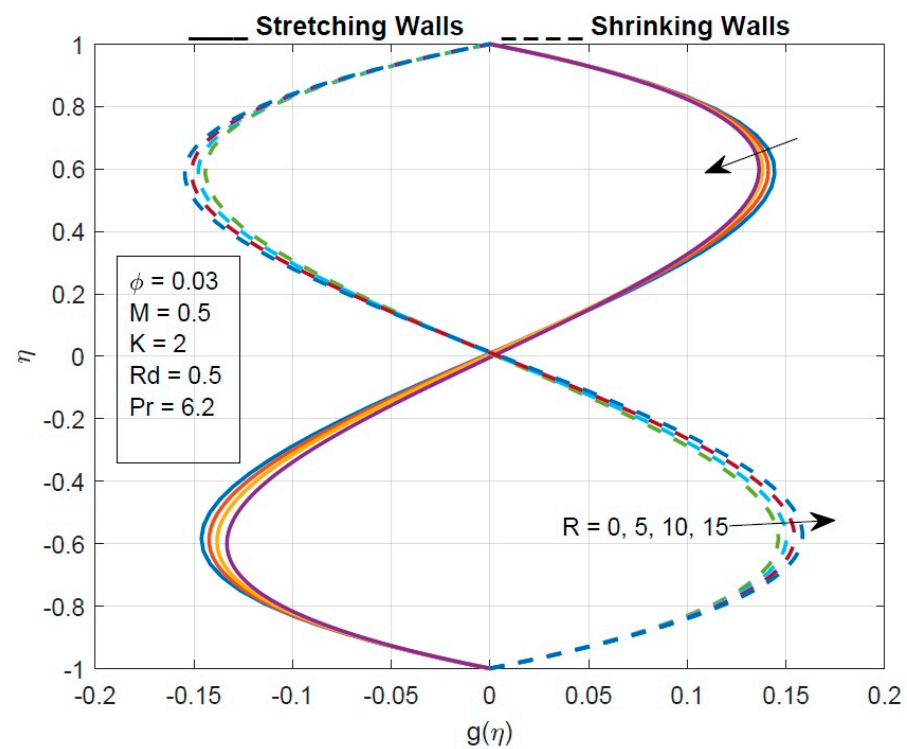


**Figure 10.** The effect of the Reynolds number on the micro-rotation profile.

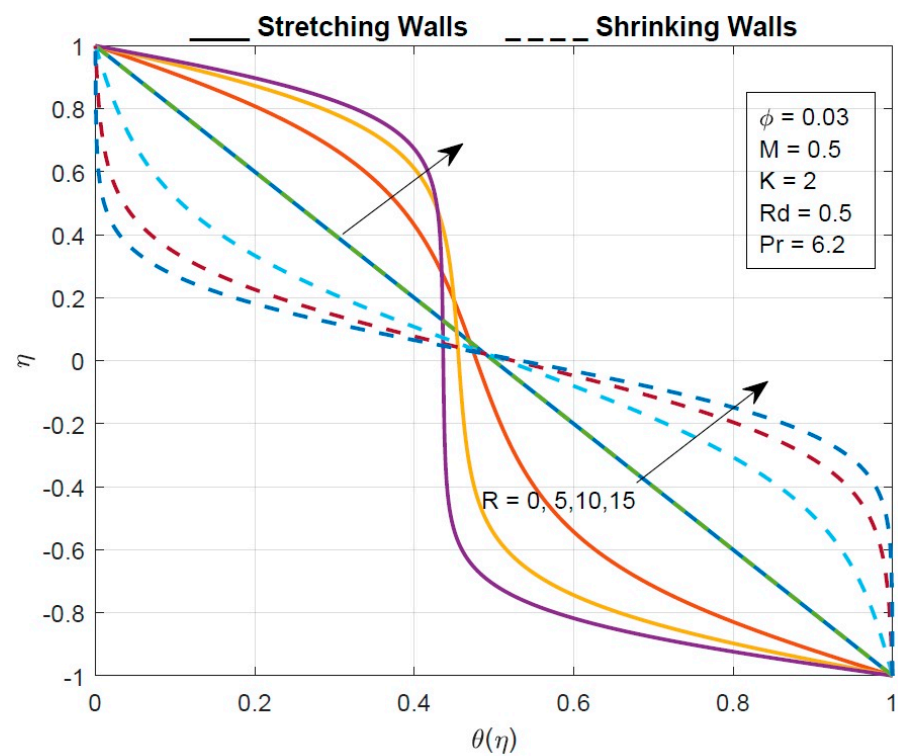


**Figure 11.** The effect of the Reynolds number on the temperature profile.

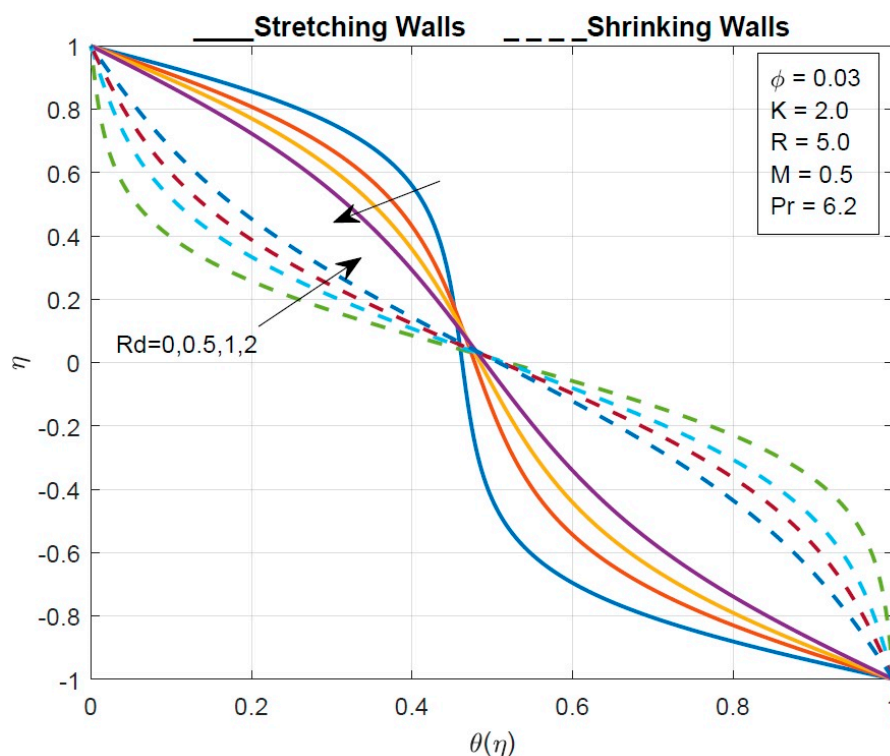


**Figure 12.** The effect of the radiation parameter on the temperature profile.

### 3.1. Application of Response Surface Methodology (RSM)

#### 3.1.1. Optimization Process

RSM is one of many useful tools for describing a wide range of variables, together with limited resources, quantitative data, and the required test design (response surface methodology). The following steps were taken into account in this process:

1. To reach the suitable and believable requirements for the intended response, we planned and investigated the data values.
2. We outlined the most appropriate mathematical models for the response surface.
3. We described the mathematical models for the response surface that are most suited.
4. We used an analysis of the variance to examine the parametric direct and interaction impacts (ANOVA).

#### 3.1.2. Optimization Analysis by RSM

The relation between the factor variables and the response variable (temperature gradient) was investigated using a face-centred central composite design. Tables 2 and 3 indicates the three factors and their levels. The quadratic model is presented in Equation (22), where three linear, square, and interactive terms are involved.

$$\text{Response} = \alpha_0 + \alpha_1 A + \alpha_2 B + \alpha_3 C + \alpha_{11} A^2 + \alpha_{22} B^2 + \alpha_{33} C^2 + \alpha_{12} AB + \alpha_{13} AC + \alpha_{23} BC \quad (22)$$

**Table 2.** Parameters with their levels for  $Cf_x(-1)$ .

Parameters	Symbols	Level		
		−1	0	1
$R$	$A$	−5	2	5
$M$	$B$	0	1	1.5
$K$	$C$	0.1	1	2

**Table 3.** Parameters with their levels  $Nu_x(-1)$ .

Parameters	Symbols	Level		
		−1	0	1
$R$	A	−5	2	5
$\varphi$	B	0	0.05	0.2
$Rd$	C	0.1	1	2

Here (Equation (22)),  $\alpha_i$  and  $\alpha_{ij}$  represent the regression coefficients. The statistical analysis was performed for 20 runs, as prescribed by the defined conditions.

$$Cf_x(-1) = 3.0015 + 0.08816R + 0.1126M - 0.1056K + 0.000686R^2 + 0.0843M^2 + 0.0479K^2 - 0.00175RM - 0.02615RK - 0.0731MK \quad (23)$$

$$Nu_x(-1) = 0.758 + 0.1441R - 2.00\varphi - 0.288Rd + 0.00412R^2 + 3.64\varphi^2 + 0.0665Rd^2 - 0.2273R\varphi - 0.03759Rd.R + 0.614\varphi Rd \quad (24)$$

The values of skin friction coefficient and Nusselt number for coded values are given in Table 4. The ANOVA Tables 5 and 6 provide a measure of accuracy for the approximate model. A parameter is important when the  $p$ -value is less than 0.05 (with 95 percent confidence). Since the  $p$ -value in the model is greater than 0.05, the linear, quadratic, and interaction terms may be omitted. Nonetheless, as seen in Table 5,6 the model proves to be superior since its coefficient of determination  $R^2$  is higher. The correct regression equation is now as follows:

$$Cf_x(-1) = 3.0015 + 0.08816R + 0.1126M - 0.1056K + 0.0843M^2 + 0.0479K^2 - 0.02615RK - 0.0731MK \quad (25)$$

$$Nu_x(-1) = 0.758 + 0.1441R - 0.288Rd - 0.03759Rd.R \quad (26)$$

**Table 4.** Experimental design and responses.

Runs	Coded Values			Response $Cf_x(-1)$	Response $Nu_x(-1)$
	A	B	C		
1	−1	−1	−1	2.569977654	0.039218876
2	1	−1	−1	3.4412049	1.706219612
3	−1	1	−1	2.931369225	0.182650354
4	1	1	−1	3.797708428	0.975161305
5	−1	−1	1	2.808665994	0.256515544
6	1	−1	1	3.173524221	0.828662877
7	−1	1	1	2.954689881	0.315102036
8	1	1	1	3.315963627	0.717271607
9	−1	0	0	2.832551727	0.185583893
10	1	0	0	3.347006534	0.981815599
11	0	−1	0	3.092057592	0.701100814
12	0	1	0	3.302840544	0.617231054
13	0	0	−1	3.340485946	0.860674809
14	0	0	1	3.124384046	0.614658362
15	0	0	0	3.187362637	0.679561304
16	0	0	0	3.187362637	0.679561304
17	0	0	0	3.187362637	0.679561304
18	0	0	0	3.187362637	0.679561304
19	0	0	0	3.187362637	0.679561304
20	0	0	0	3.187362637	0.679561304

Table 5. ANOVA for  $Cf_x(-1)$ .

Source	DF	Adjusted Sum of Square	Adjusted Mean Square	F-Value	p-Value	Remarks
Model	9	1.27499	0.141666	211.26	0.000	Significant
Linear	3	1.05111	0.350369	522.48	0.000	Significant
R	1	0.87703	0.877027	1307.85	0.000	Significant
M	1	0.14695	0.146950	219.14	0.000	Significant
K	1	0.03201	0.032010	47.73	0.000	Significant
Square	3	0.03435	0.011451	17.08	0.000	Significant
R.R	1	0.00055	0.000546	0.81	0.388	Not Significant
M.M	1	0.00474	0.004738	7.07	0.024	Significant
K.K	1	0.00509	0.005093	7.59	0.020	Significant
2-Way Interaction	3	0.15276	0.050919	75.93	0.000	Significant
R.M	1	0.00036	0.000362	0.54	0.480	Not Significant
R.K	1	0.12739	0.127394	189.97	0.000	Significant
M.K	1	0.02220	0.022204	33.11	0.000	Significant
Error	10	0.00671	0.000671			
Lack-of-Fit	5	0.00671	0.001341	*	*	
Pure Error	5	0.00000	0.000000			
Total	19	1.28170				
$R^2 = 99.48\%$		Adjusted $R^2 = 99.01\%$				

Table 6. ANOVA for  $Nu_x(-1)$ .

Source	DF	Adj SS	Adj MS	F-Value	p-Value	Remarks
Model	9	2.39452	0.26606	26.11	0.000	Significant
Linear	3	1.76127	0.58709	57.62	0.000	Significant
R	1	1.65970	1.65970	162.90	0.000	Significant
Phi	1	0.03905	0.03905	3.83	0.079	Not Significant
Rd	1	0.06770	0.06770	6.64	0.028	Significant
Square	3	0.09999	0.03333	3.27	0.067	Not Significant
R.R	1	0.01970	0.01970	1.93	0.194	Not Significant
Phi.Phi	1	0.00191	0.00191	0.19	0.674	Not Significant
Rd.Rd	1	0.00982	0.00982	0.96	0.349	Not Significant
2-Way Interaction	3	0.41288	0.13763	13.51	0.001	Significant
R.Phi	1	0.11203	0.11203	11.00	0.008	Not Significant
R.Rd	1	0.26292	0.26292	25.81	0.000	Significant
Phi.Rd	1	0.02855	0.02855	2.80	0.125	Not Significant
Error	10	0.10188	0.01019			
Lack-of-Fit	5	0.10188	0.02038	*	*	
Pure Error	5	0.00000	0.00000			
Total	19	2.49640				
$R^2 = 95.92\%$		Adjusted $R^2 = 92.25\%$				

Tables 2 and 3 present the various levels of the parameters for  $Cf_x(-1)$  and  $Nu_x(-1)$ , respectively. However, Table 4 represents the values of the response function for 20 different points. In Tables 5 and 6, the  $R^2$  for  $Cf_x(-1)$  and  $Nu_x(-1)$  (99.48% and 95.92% respectively), which was obtained by the testing methods and statistical analysis of the model, is presented. However, the  $R^2$ -adj amounts for  $Cf_x(-1)$  and  $Nu_x(-1)$  (99.01% and 92.25%, respectively) are  $\leq R^2$ , but the model fits the data reasonably [30–33]. Moreover, the importance of the model for the response variables  $Cf_x(-1)$  and  $Nu_x(-1)$  is depicted from the F-value, which is equal to 211.26 and 26.11, respectively. According to Figure 13a,b, it is observed that the plots of normal probability are well-behaved and in good condition [33]. From these two figures, the residual histograms exhibit a skewed distribution. When the residual diagrams and fitted values were compared, the observed and fitted values showed a strong correlation.

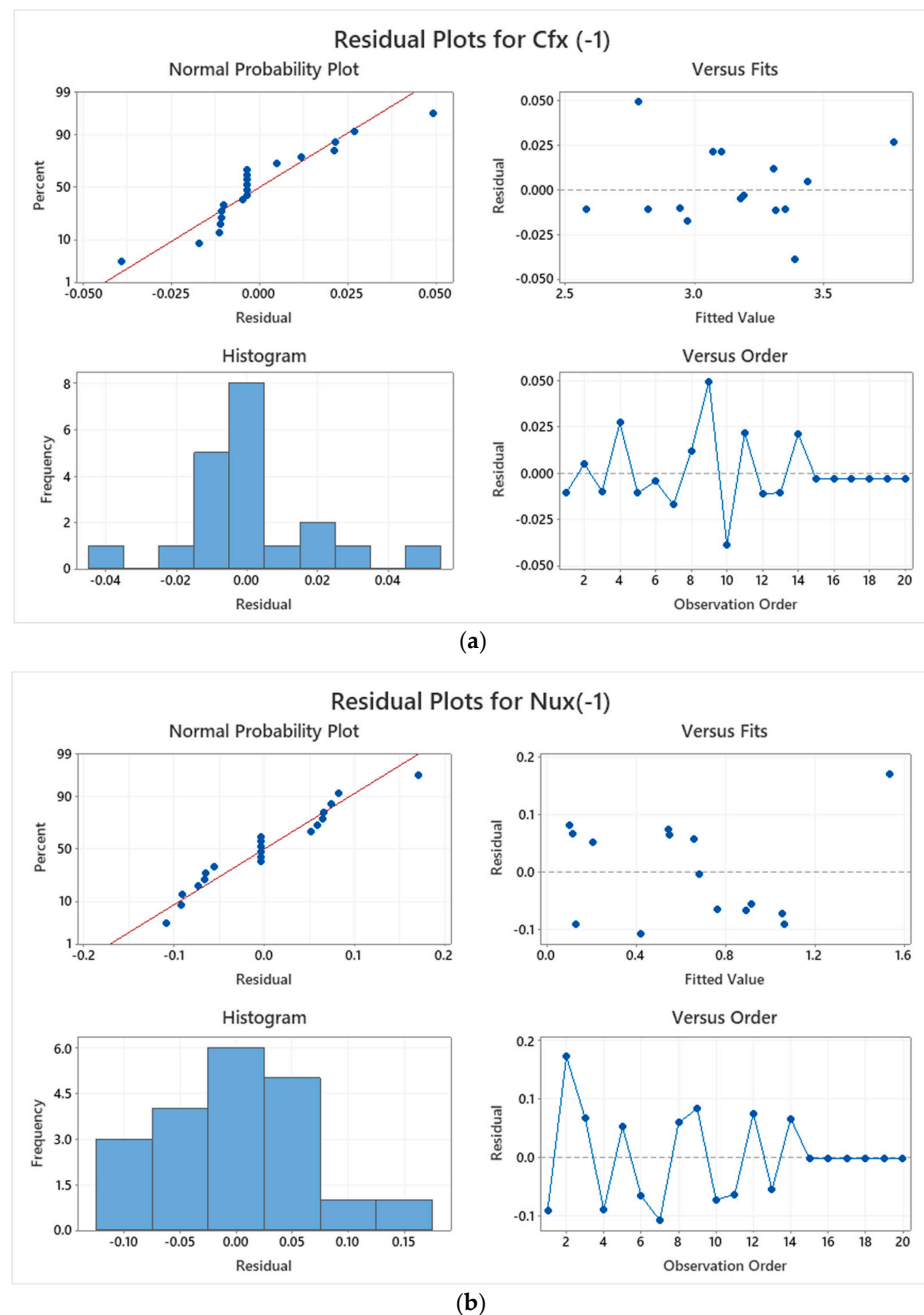


Figure 13. Residual plot for (a)  $C_{fx}$  (b).

Figures 14 and 15 show the mean total skin friction coefficient and Nusselt number variations as effective parameters functions. The deviation of the skin friction coefficient in terms of  $M$  and  $R$  are shown in Figure 14a. The skin friction coefficient increases as  $M$  and  $R$  are increased, with the highest value (+1) and lowest value (−1) for  $M$  and  $R$ , respectively. The variation in the response variable (skin friction) with respect to  $K$  and  $R$  are shown in Figure 14b. It is observed that reducing the values of  $K$  and increasing the value of  $R$  causes an increase in the skin friction coefficient. The highest value of skin friction is obtained in the level of (−1) and (+1) and its lowest value is observed in the level of (+1) and (+1) for  $K$  and  $R$ , respectively. The variance of the skin friction coefficient in terms of  $K$  and  $M$  is shown in Figure 14c. The skin friction is increased when the value of  $K$  is reduced and the value of  $M$  is increased. Furthermore, for  $K$  and  $M$ , the highest and lowest values of the skin friction coefficient can be found at the levels of (−1) and (+1), respectively. The variance of the total Nusselt number in terms of the solid volume fraction of a nanofluid

and the Reynolds number  $R$  is shown in Figure 15a. The Nusselt number is increased when the solid volume fraction is lower and the Reynolds number is higher. Moreover, the Nusselt number gains its minimum value in  $(+1)$  and  $(-1)$  and its maximum in  $(-1)$  and  $(+1)$  for  $\varphi$  and  $R$ , respectively. Figure 15b shows that the Nusselt number increases by increasing the values of  $R$  and decreasing the values of  $Rd$ . Nevertheless, the Nusselt number gains a maximum in level  $(-1)$  and  $(+1)$  and a minimum in  $(+1)$  and  $(-1)$  for  $Rd$  and  $R$ , respectively. In the same vein, Figure 15c shows that the Nusselt number reaches its highest value in  $(-1)$  and  $(-1)$  and its lowest value in  $(+1)$  and  $(+1)$  for  $Rd$  and the solid volume fraction.

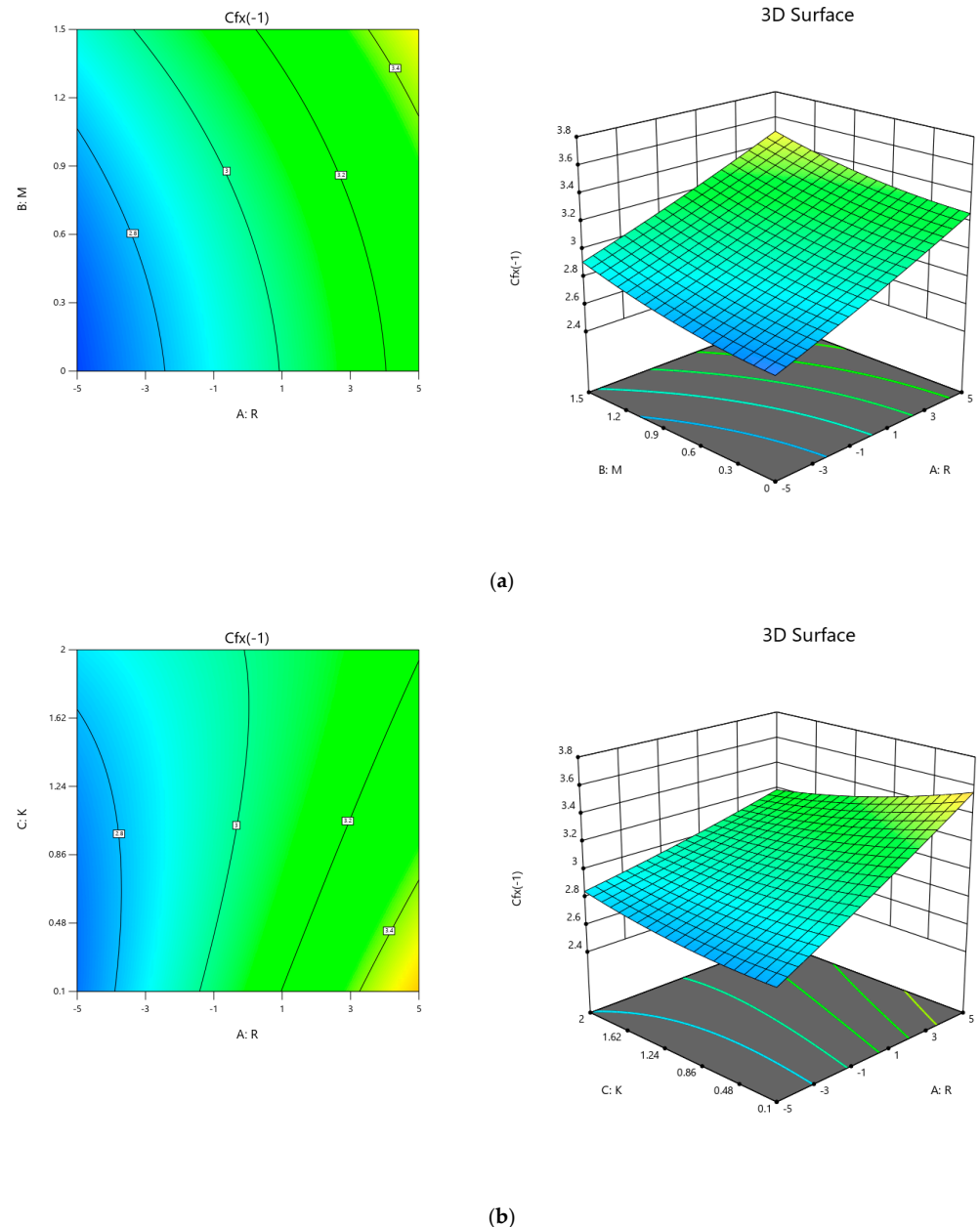
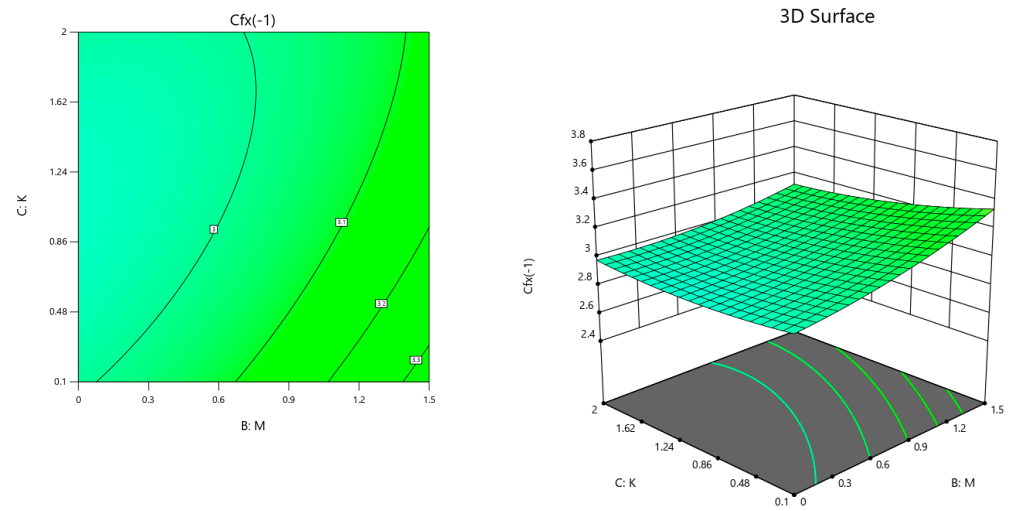


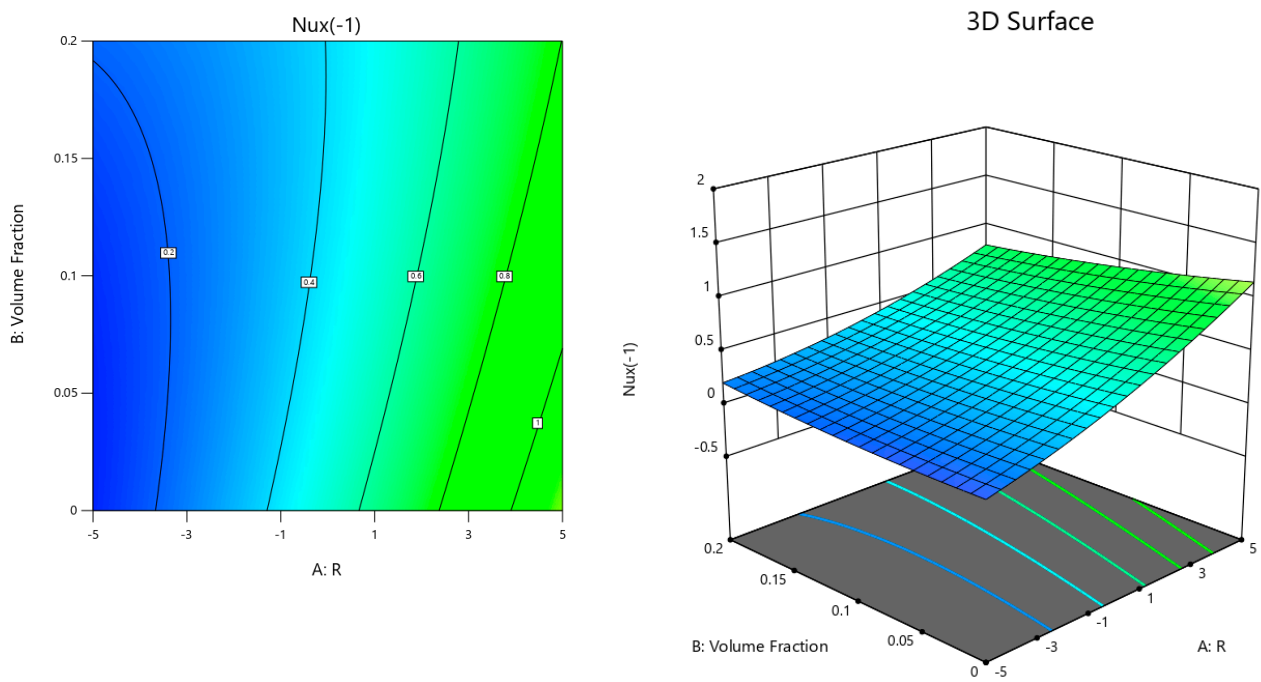
Figure 14. Cont.





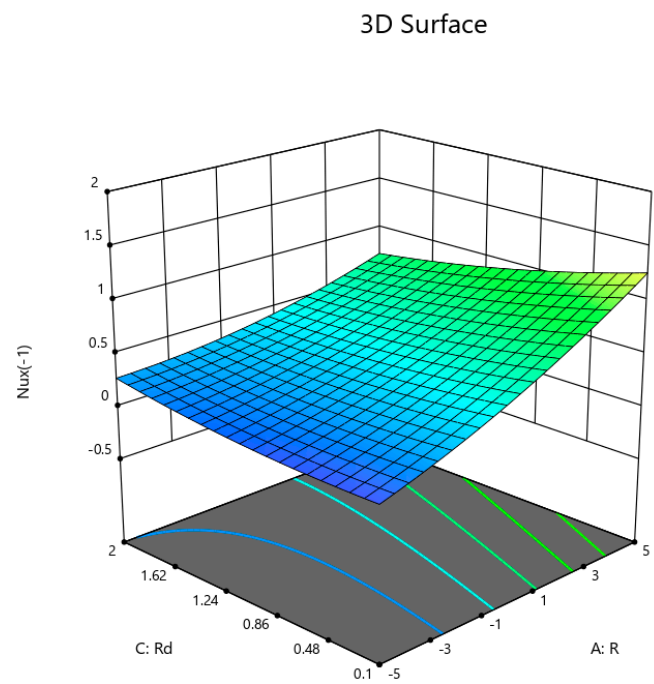
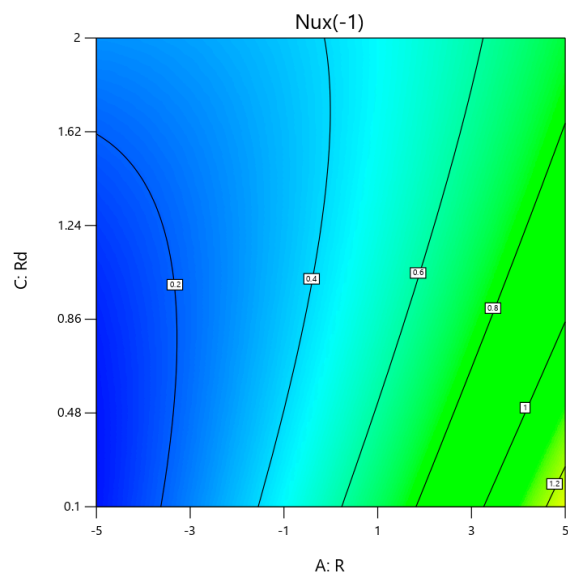
(c)

**Figure 14.** Three-dimensional surfaces and contour plots for all continuous parameters of  $M$ ,  $R$ , and  $K$  on  $Cfx$ .

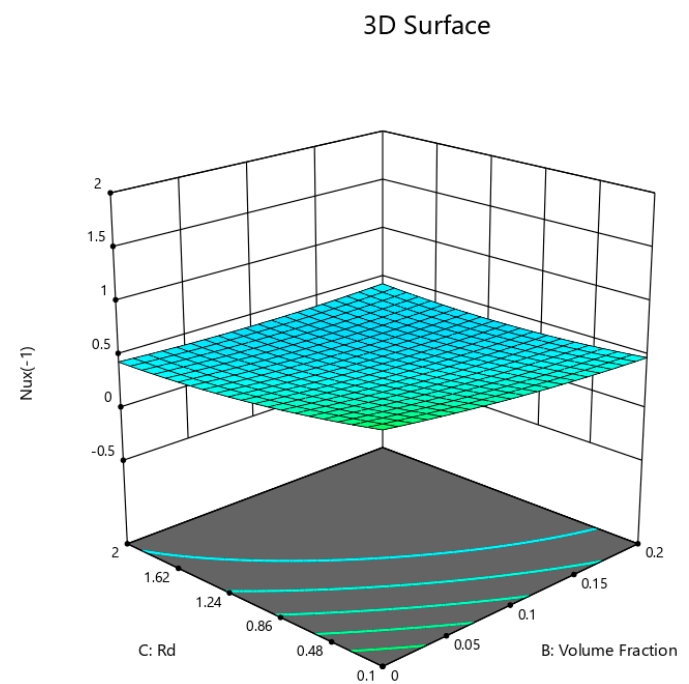
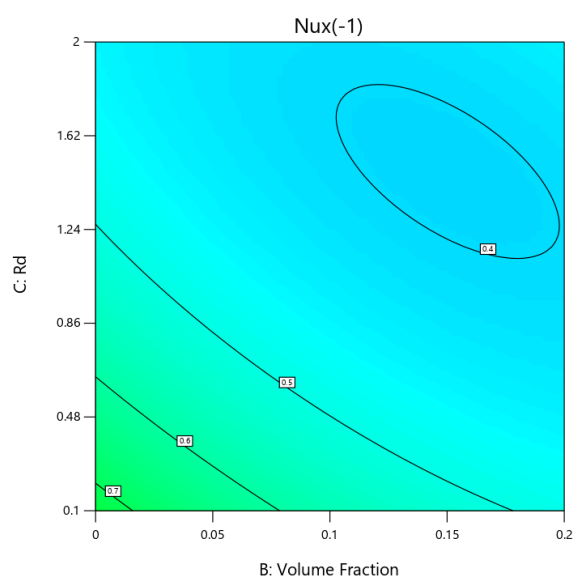


(a)

**Figure 15.** Cont.



(b)



(c)

**Figure 15.** Three-dimensional surfaces and contour plots for all continuous parameters of  $R$ ,  $\Phi$ , and  $Rd$  on  $Nux$ .

The regression Equations (25) and (26) are used to calculate the sensitivity. The sensitivity functions are the partial derivatives of the response variables with respect to the factor variables, as shown below:

$$\frac{\partial Cf_x}{\partial A} = 0.08816 - 0.02615K \quad (27)$$

$$\frac{\partial Cf_x}{\partial B} = 0.1126 + 0.1686M - 0.0731K \quad (28)$$

$$\frac{\partial Cf_x}{\partial C} = -0.1056 + 0.0958K - 0.02615R - 0.0731M \quad (29)$$

$$\frac{\partial Nu_x}{\partial A} = 0.1441 - 0.03759Rd \quad (30)$$

$$\frac{\partial Nu_x}{\partial B} = 0 \quad (31)$$

$$\frac{\partial Nu_x}{\partial C} = -0.288 - 0.03759R \quad (32)$$

The positive sensitivity value indicates that the objective function has improved as a result of the improved input parameters. Its negative value, on the other hand, denotes a decline in the objective function due to the increased input parameters. From Table 7, it is seen that the sensitivity of  $Cf_x$  to A and B is positive and negative for C. Similarly, from Table 8, the sensitivity of  $Nu_x$  to A is positive and negative for C.

**Table 7.** Sensitivity analysis of the response  $Cf_x$ .

A	B	C	Sensitivity to A	Sensitivity to B	Sensitivity to C
0	−1	−1	0.11431	0.0171	−0.1283
0	−1	0	0.08816	−0.056	−0.0325
0	−1	1	0.06201	−0.1291	0.0633
0	0	−1	0.11431	0.1857	−0.2014
0	0	0	0.08816	0.1126	−0.1056
0	0	1	0.06201	0.0395	−0.0098
0	1	−1	0.11431	0.3543	−0.2745
0	1	0	0.08816	0.2812	−0.1787
0	1	1	0.06201	0.2081	−0.0829

**Table 8.** Sensitivity analysis of the response  $Nu_x$ .

A	B	C	Sensitivity to A	Sensitivity to B	Sensitivity to C
−1	0	−1	0.18169	0	−0.25041
−1	0	0	0.1441	0	−0.25041
−1	0	1	0.10651	0	−0.25041
0	0	−1	0.18169	0	−0.288
0	0	0	0.1441	0	−0.288
0	0	1	0.10651	0	−0.288
1	0	−1	0.18169	0	−0.32559
1	0	0	0.1441	0	−0.32559
1	0	1	0.10651	0	−0.32559

#### 4. Conclusions

In this investigation, we considered two-dimensional steady laminar incompressible micropolar nanofluid in a channel with stretching and shrinking walls in the presence of a magnetic field and thermal radiation. The copper nanoparticles are the solid dispersed phase, while blood is the fluid continuum phase. The lower and upper walls of the channel stretch and shrink in the direction of the fluid (x-axis). The governing similar ODEs were

solved and verified by two different numerical schemes. After in-depth discussions of the model, the main findings are drawn as below:

- The velocity of the fluid particles decreases by increasing the values of the micropolar parameter.
- As the radiation parameter increases, the temperature profile decreases from the lower wall to the middle and increases from the centre to the upper wall of the tube.
- The velocity profile declines as a solid volume fraction  $\phi$  enhances for the stretching walls and increases for the shrinking walls.
- The skin friction coefficient increases as the magnetic and Reynolds number are increased.
- The Nusselt number is increased when the solid volume fraction is lower.
- The sensitivity of  $Cf_x$  to the Reynolds number and magnetic parameter is positive and negative for the micropolar parameter.
- $Nu_x$  is optimized by taking higher values of the Reynolds number and lower values of the radiation parameter.

**Author Contributions:** Conceptualization, J.R. and T.M.; Methodology, R.A.A. and S.A.M.A.; Software, J.R., T.M., M.R.G. and A.M.H.; Validation, R.A.A. and M.R.G.; Formal analysis, S.A.M.A.; Investigation, M.R.G.; Resources, J.R. and A.M.H.; Data curation, T.M., S.A.M.A. and A.M.H.; Writing—original draft, J.R. and T.M.; Writing—review & editing, R.A.A. All authors have read and agreed to the published version of the manuscript.

**Funding:** Princess Nourah bint Abdulrahman University Researchers Supporting Project number (PNURSP2023R61), Princess Nourah bint Abdulrahman University, Riyadh, Saudi Arabia.

**Data Availability Statement:** Not applicable.

**Acknowledgments:** The authors express their gratitude to Princess Nourah bint Abdulrahman University Researchers Supporting Project number (PNURSP2023R61), Princess Nourah bint Abdulrahman University, Riyadh, Saudi Arabia.

**Conflicts of Interest:** The authors declare no conflict of interest.

## References

1. Eringen, A.C. Theory of micropolar fluids. *J. Math. Mech.* **1966**, *16*, 1–18. [\[CrossRef\]](#)
2. Eringen, A.C. Theory of micropolar elasticity. In *Microcontinuum Field Theories*; Springer: New York, NY, USA, 1999; pp. 101–248.
3. Mohammadein, A.A.; Gorla, R.S.R. Effects of transverse magnetic field on mixed convection in a micropolar fluid on a horizontal plate with vectored mass transfer. *Acta Mech.* **1996**, *118*, 1–12. [\[CrossRef\]](#)
4. Peddieson, J. Boundary Layer Theory for a Micropolar Fluid. 1970. Available online: [web](#) (accessed on 1 January 2023).
5. Gupta, P.S.; Gupta, A.S. Heat and mass transfer on a stretching sheet with suction or blowing. *Can. J. Chem. Eng.* **1977**, *55*, 744–746. [\[CrossRef\]](#)
6. Chakrabarti, A.; Gupta, A.S. Hydromagnetic flow and heat transfer over a stretching sheet. *Q. Appl. Math.* **1979**, *37*, 73–78. [\[CrossRef\]](#)
7. Incropera, F.P.; Bergman, T.L.; Lavine, A.S.; DeWitt, D.P. *Fundamentals of Heat and Mass Transfer*; Springer: New York, NY, USA, 2011.
8. Cengel, Y.A.; Boles, M.A. *Thermodynamics: An Engineering Approach*, 8th ed.; McGraw-Hill: New York, NY, USA, 2015.
9. Cengel, Y.A. *Heat Transfer: A Practical Approach*, 2nd ed.; McGraw-Hill: New York, NY, USA, 2002.
10. Zhao, N.; Li, S.; Yang, J. A review on nanofluids: Data-driven modeling of thermalphysical properties and the application in automotive radiator. *Renew Sustain. Energy Rev.* **2016**, *66*, 596–616. [\[CrossRef\]](#)
11. Krishna, V.M.; Kumar, M.S. Numerical analysis of forced convective heat transfer of nanofluids in microchannel for cooling electronic equipment. *Mater. Today Proc.* **2019**, *17*, 295–302. [\[CrossRef\]](#)
12. Okonkwo, E.C.; Okwose, C.F.; Abid, M.; Ratlamwala, T.A.H. Second-law analysis and exergoeconomics optimization of a solar tower—Driven combined-cycle power plant using supercritical CO<sub>2</sub>. *J. Energy Eng. ASCE* **2018**, *144*, 04018021. [\[CrossRef\]](#)
13. Okonkwo, E.C.; Abid, M.; Ratlamwala, T.A.H. Numerical analysis of heat transfer enhancement in a parabolic trough collector based on geometry modifications and working fluid usage. *J. Sol. Energy Eng.* **2018**, *140*, 0510091. [\[CrossRef\]](#)
14. Meseguer, J.; Pérez-Grande, I.; Sanz-Andrés, A. *Spacecraft Thermal Control*, 1st ed.; Elsevier: London, UK, 2012.
15. Sajid, M.U.; Ali, H.M. Thermal conductivity of hybrid nanofluids: A critical review. *Int. J. Heat Mass Transf.* **2018**, *126*, 211–234. [\[CrossRef\]](#)

16. Das, S.K.; Choi, S.U.S.; Patel, H.E. Heat transfer in nanofluids—A review heat transfer in nanofluids. *Heat Transf. Eng.* **2007**, *27*, 37–41.
17. Choi, S.U.; Eastman, J.A. *Enhancing Thermal Conductivity of Fluids with Nanoparticles*; No. ANL/MSD/CP-84938; CONF-951135-29; Argonne National Lab.: Lemont, IL, USA, 1995.
18. Liu, L.H.; Métivier, R.; Wang, S.; Wang, H. Advanced nanohybrid materials: Surface modification and applications. *J. Nanomater.* **2012**, *2012*, 536405. [[CrossRef](#)]
19. Rashid, I.; Haq, R.U.; Al-Mdallal, Q.M. Aligned magnetic field effects on water based metallic nanoparticles over a stretching sheet with PST and thermal radiation effects. *Phys. E Low-Dimens. Syst. Nanostruct.* **2017**, *89*, 33–42. [[CrossRef](#)]
20. ul Haq, R.; Aman, S. Water functionalized CuO nanoparticles filled in a partially heated trapezoidal cavity with inner heated obstacle: FEM approach. *Int. J. Heat Mass Transf.* **2019**, *128*, 401–417. [[CrossRef](#)]
21. Hayat, T.; Imtiaz, M.; Alsaedi, A. Melting heat transfer in the MHD flow of Cu–water nanofluid with viscous dissipation and Joule heating. *Adv. Powder Technol.* **2016**, *27*, 1301–1308. [[CrossRef](#)]
22. Sandeep, N.; Sharma, R.P.; Ferdows, M. Enhanced heat transfer in unsteady magnetohydrodynamic nanofluid flow embedded with aluminum alloy nanoparticles. *J. Mol. Liq.* **2017**, *234*, 437–443. [[CrossRef](#)]
23. Shah, F.; Khan, M.I.; Hayat, T.; Khan, M.I.; Alsaedi, A.; Khan, W.A. Theoretical and mathematical analysis of entropy generation in fluid flow subject to aluminum and ethylene glycol nanoparticles. *Comput. Methods Programs Biomed.* **2019**, *182*, 105057. [[CrossRef](#)] [[PubMed](#)]
24. Misra, J.C.; Shit, G.C.; Rath, H.J. Flow and heat transfer of a MHD viscoelastic fluid in a channel with stretching walls: Some applications to haemodynamics. *Comput. Fluids* **2008**, *37*, 1–11. [[CrossRef](#)]
25. Ashraf, M.; Jameel, N.; Ali, K. MHD non-Newtonian micropolar fluid flow and heat transfer in channel with stretching walls. *Appl. Math. Mech.* **2013**, *34*, 1263–1276. [[CrossRef](#)]
26. Raza, J.; Rohni, A.M.; Omar, Z. MHD flow and heat transfer of Cu–water nanofluid in a semi porous channel with stretching walls. *Int. J. Heat Mass Transf.* **2016**, *103*, 336–340. [[CrossRef](#)]
27. Reza, J.; Mebarek-Oudina, F.; Makinde, O.D. MHD slip flow of Cu-Kerosene nanofluid in a channel with stretching walls using 3-stage Lobatto IIIA formula. In *Defect and Diffusion Forum*; Trans Tech Publications Ltd.: Wollerau, Switzerland, 2018; Volume 387, pp. 51–62.
28. Raza, J.; Rohni, A.M.; Omar, Z. Numerical investigation of copper-water (Cu-water) nanofluid with different shapes of nanoparticles in a channel with stretching wall: Slip effects. *Math. Comput. Appl.* **2016**, *21*, 43. [[CrossRef](#)]
29. Lund, L.A.; Omar, Z.; Raza, J.; Khan, I. Magnetohydrodynamic flow of Cu–Fe 3 O 4 /H 2 O hybrid nanofluid with effect of viscous dissipation: Dual similarity solutions. *J. Therm. Anal. Calorim.* **2021**, *143*, 915–927. [[CrossRef](#)]
30. Chan, S.Q.; Aman, F.; Mansur, S. Sensitivity analysis on thermal conductivity characteristics of a water-based bionanofluid flow past a wedge surface. *Math. Probl. Eng.* **2018**, *2018*, 9410167. [[CrossRef](#)]
31. Vahedi, S.M.; Pordanjani, A.H.; Raisi, A.; Chamkha, A.J. Sensitivity analysis and optimization of MHD forced convection of a Cu-water nanofluid flow past a wedge. *Eur. Phys. J. Plus* **2019**, *134*, 124. [[CrossRef](#)]
32. Khan, N.S.; Kumam, P.; Thounthong, P. Second law analysis with effects of Arrhenius activation energy and binary chemical reaction on nanofluid flow. *Sci. Rep.* **2020**, *10*, 19792. [[CrossRef](#)]
33. Thriveni, K.; Mahanthesh, B. Significance of variable fluid properties on hybrid nanoliquid flow in a micro-annulus with quadratic convection and quadratic thermal radiation: Response surface methodology. *Int. Commun. Heat Mass Transf.* **2021**, *124*, 105264. [[CrossRef](#)]

**Disclaimer/Publisher’s Note:** The statements, opinions and data contained in all publications are solely those of the individual author(s) and contributor(s) and not of MDPI and/or the editor(s). MDPI and/or the editor(s) disclaim responsibility for any injury to people or property resulting from any ideas, methods, instructions or products referred to in the content.